The meandering orbit effect of the tilting instability in configuration

journal or publication title	Physics of Fluids B
volume	Vol.2
number	No.11
page range	pp.2652-2660
year	1990-11-01
URL	http://hdl.handle.net/10655/1304

doi: 10.1063/1.859579

The meandering orbit effect on stabilization of the tilting instability in a field-reversed configuration

Ritoku Horiuchi[a)]
Science Project Corporation, Kuchita-Mimami 3-40-17-304, Asakita-Ku, Hiroshima 739-19, Japan
Tetsuya Sato
National Institute for Fusion Science, Nagoya 464-01, Japan

(Received 29 January 1990; accepted 1 June 1990)

The ion kinetic effect in the tilt disruption of a field-reversed configuration is investigated by means of a three-dimensional particle simulation. It is found that the tilt disruption is completely suppressed when $\bar{s} \approx 1$, where $\bar{s}$ measures the number of ion gyroradii over the radial distance between the magnetic separatrix line and the field-null line. A prolate magnetic well is formed around the field-null line, in which ions do not execute gyration but meander along the field-null line. For the case of $\bar{s} \approx 1$ a large number of ions exist in the magnetic well and move on stable orbits around the major axis with an average rotation velocity nearly equal to half the thermal velocity. As $\bar{s}$ becomes larger than 1, the number of ions in the magnetic well decreases and the stabilization effect is reduced. It is also found that an anisotropy is created in the ion thermal pressure profile owing to the anisotropy of the meandering orbits and that the electric field fluctuation always remains at a low level, and thus the electric field plays no essential role in the tilt stabilization.

I. INTRODUCTION

The field-reversed configuration (FRC) is a compact toroidal device in which a high-beta plasma is confined by a simple magnetic geometry with a negligible toroidal magnetic field. The characteristic features, i.e., simple geometry and high-beta plasma, make the FRC attractive as a magnetic fusion device. However, it is pointed out that there exist two global instabilities leading to the destruction of plasma confinement. One is the $n = 2$ rotational instability, where n is the toroidal mode number. This instability was found to be suppressed by applying external multipole fields.[1] The other is the $n = 1$ tilting instability.[2-4] However, no experimental evidence has so far been reported on the tilt disruption in the magnetohydrodynamic (MHD) time scale predicted by linear analysis.[1,5] Two possibilities are conceivable to explain the discrepancy between linear theory and experiment. The first explanation is that the nonlinear saturation mechanism could protect the FRC plasma from the destructive growth of the tilt mode. Horiuchi and Sato[6] have carried out a three-dimensional full MHD simulation and found no evidence for the nonlinear saturation of the tilt mode except for a highly spinning case.

An alternative explanation may be given by taking into account the ion kinetic effect. That is, the stabilization effect resulting from the ion finite-Larmor radius (FLR) can operate effectively in current devices since the device scale is comparable to the ion Larmor radius. Barnes *et al.*[7] derived the linear growth rate from the Vlasov-fluid dispersion equations and found that the tilt mode could be stabilized for a large gyroradius case of $\bar{s} \leqslant 2$, where $\bar{s}$ is defined by

$$\bar{s} = \int_{r_a}^{r_s} \frac{r\,dr}{r_s \lambda_i}, \tag{1}$$

where r_s is the separatrix radius, r_a is the radius of the magnetic null, and λ_i is the local ion gyroradius. By using a two-fluid variation formalism, Ishida *et al.*[8] have shown that a stabilization region would appear for a very highly prolate and small $\bar{s}$ case as a result of the effect of the Hall term. Milroy *et al.*[9] have examined the ion kinetic effect by solving the nonlinear MHD equations, including the Hall term. Their results indicate that the Hall term can reduce the growth rate of the tilt mode for the highly prolate and small $\bar{s}$ case. However, their analyses cannot fully explain the discrepancy between theory and experiment.[10] This is probably because the Hall term can represent only a part of the ion FLR effect. Particularly in the case where the field-null region exists, inclusion of the Hall term in the MHD equations is insufficient in dealing with the whole FLR effect.

One of the characteristic features of the FRC plasma is that a field-null line exists in the central plasma region because of the strong toroidal plasma current. For a device with $\bar{s} \approx 1$ most of the particles in the vicinity of the field-null line cannot make gyration motions, but reveal complex behaviors.[11] For reference, we show eight types of ion orbit in Fig. 1 for a one-dimensional model in which the magnetic field has only the z component and its value depends only on the coordinate x in the form $B_z(x) = B_0(x/x_0)$; x_0 is the scale height and B_0 is the characteristic value of the magnetic field. An ion is pushed in the negative y direction with a velocity v_y from the initial point $(x_0, 0)$. For the case of the normalized Larmor radius $\lambda_i/x_0 = 0.22$ ions move along the gradient-**B** drift orbit. When $\lambda_i/x_0 > 0.25$ ions move across the field-null line and their orbits form a combined shape of two gradient-**B** drift orbits (figure-eight shaped orbits). When the gyration velocity is larger than the critical one ($\lambda_i/x_0 > 0.303$), the ions drift in the direction opposite

[a)] Present address: National Institute for Fusion Science, Nagoya 464-01, Japan.

 0899-8221/90/112652-09$02.00

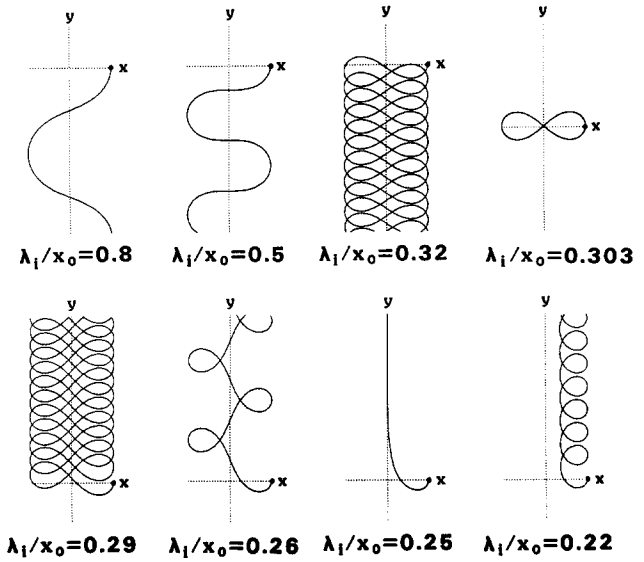

FIG. 1. Eight types of ion orbit in the one-dimensional neutral sheet model. The magnetic field has only the z component and its value depends only on the coordinate x in the form $B_z(x) = B_0(x/x_0)$, where x_0 is the scale height and B_0 is the characteristic value of the magnetic field. The solid curve shows the ion trajectory that starts with a negative velocity $-v_y$ from the point $(x_0,0)$.The Larmor radius λ_i at the starting point is given by $v_y/(q_iB_0/m_ic)$ with a particle mass m_i and a particle charge q_i.

to that of the gradient-**B** drift. As the velocity (energy) increases further, ions execute meandering motions along a field-null line without any self-intersection of the orbit line ($\lambda_i/x_0 = 0.8$). In this way it is important to take into account the effect of the finite-sized particle orbit in the real magnetic geometry on the global behavior of the FRC plasma.

The best way to investigate the FLR stabilization effect against the tilting instability is to carry out a macroscale particle simulation that can describe both the electron and ion FLR effects and the global behavior over the device scale simultaneously.[12,13] For this purpose we use a three-dimensional macroscale particle simulation code in the cylindrical coordinates, which relies on the semi-implicit scheme. The initial condition and the simulation model are described in Sec. II. The results obtained from the particle simulation are discussed in comparison with the MHD result in Sec. III. The first half of Sec. III is devoted to discussions of the ion kinetic stabilization effect in connection with the character of the meandering orbit. We also discuss the anisotropy of the ion pressure profile and the $\bar{s}$ dependence of the plasma rotation in the latter half of Sec. III. Finally, we give a brief discussion of the electric field and the applicability of the model in Sec. IV.

II. SIMULATION MODEL

It should be emphasized that not only ions but also electrons reveal fairly complex behaviors near the field-null point and the sharply curved edges of field lines in the FRC plasma. Thus we must rely on a simulation study that can adequately treat the nonlinear interaction between the electron thermal motion and the fluctuating field in real geometry.

We study the FRC plasma in a cylindrical conducting vessel in which the plasma is confined by a uniform external field. The equations to be solved are the equations of motion,

$$\frac{d(\gamma_j \mathbf{v}_j)}{dt} = \frac{q_j}{m_j}\left(\mathbf{E} + \frac{\mathbf{v}_j}{c}\times\mathbf{B}\right), \tag{2}$$

$$\frac{d\mathbf{x}_j}{dt} = \mathbf{v}_j, \tag{3}$$

and the Maxwell equations,

$$\frac{1}{c}\frac{\partial \mathbf{B}}{\partial t} = -\nabla\times\mathbf{E}, \tag{4}$$

$$\frac{1}{c}\frac{\partial \mathbf{E}}{\partial t} = \nabla\times\mathbf{B} - 4\pi\mathbf{j}, \tag{5}$$

$$\nabla\cdot\mathbf{B} = 0, \tag{6}$$

$$\nabla\cdot\mathbf{E} = 4\pi\rho, \tag{7}$$

where $\mathbf{x}_j(t)$, $\mathbf{v}_j(t)$, m_j, and q_j are the position, the velocity, the rest mass, and the charge of the jth particle, and the relativistic γ factor of the jth particle is defined by

$$\gamma_j = 1/\sqrt{1 - (\mathbf{v}_j\cdot\mathbf{v}_j)/c^2}. \tag{8}$$

The current density $\mathbf{j}(\mathbf{x},t)$ and the mass density $\rho(\mathbf{x},t)$ are obtained by summing over all the particles, namely,

$$\mathbf{j}(\mathbf{x},t) = \sum_{j=1}^{N} \frac{q_j\mathbf{v}_j(t)}{c}\delta[\mathbf{x} - \mathbf{x}_j(t)], \tag{9}$$

$$\rho(\mathbf{x},t) = \sum_{j=1}^{N} m_j\delta[\mathbf{x} - \mathbf{x}_j(t)], \tag{10}$$

where N is the total number of particles.

In principle, we solve the evolutional equations (2)–(5) by assigning the initial conditions $\mathbf{x}_j(0)$, $\mathbf{v}_j(0)$, $\mathbf{B}(\mathbf{x},\mathbf{0})$, and $\mathbf{E}(\mathbf{x},\mathbf{0})$, which satisfy Eqs. (6), (7), and (10). In order to investigate the global stability of the FRC plasma, we consider a two-fluid MHD equilibrium as an initial model, which is described by

$$\frac{\partial P_i}{\partial r} = n_iq_i\frac{U_i}{c}B_z + m_in_i\frac{U_i^2}{r}, \tag{11}$$

$$\frac{\partial P_i}{\partial z} = -n_iq_i\frac{U_i}{c}B_r, \tag{12}$$

$$\frac{\partial P_e}{\partial r} = n_eq_e\frac{U_e}{c}B_z, \tag{13}$$

$$\frac{\partial P_e}{\partial z} = -n_eq_e\frac{U_e}{c}B_r, \tag{14}$$

$$-\frac{\partial B_z}{\partial r} + \frac{\partial B_r}{\partial z} = -\frac{4\pi}{c}(n_iq_iU_i + n_eq_eU_e), \tag{15}$$

where the cylindrical coordinates (r,ϕ,z) are used, subscript i or e denotes ion or electron, $U_{i(e)}$ is the ϕ component of the ion (electron) fluid velocity, $P_{i(e)}$ is the ion (electron) thermal pressure, and $n_{i(e)}$ is the ion (electron) number density. In Eqs. (11)–(14) the local neutrality condition is assumed, i.e., $n_e(\mathbf{x},0) = n_i(\mathbf{x},0)$ and $\mathbf{E}(\mathbf{x},\mathbf{0}) = 0$.

Before solving Eqs. (11)–(15) let us examine the characteristic features for the case where the electron tempera-

ture is much less than the ion temperature and the diamagnetic current is wholly carried by the average ion flow. If the plasma is rigidly rotating ($U_i = r\Omega_i$) and the ion pressure P_i is in proportion to $n_i^{\alpha/(\alpha-1)}$ (α is a constant parameter), the solution is written in the form

$$T_i(r,z) = T_0[\Phi(r,z) + \tilde{r}^2/S_*^2], \tag{16}$$

$$n_i(r,z) = n_0[\Phi(r,z) + \tilde{r}^2/S_*^2]^{\alpha-1}, \tag{17}$$

$$P_i(r,z) = P_0[\Phi(r,z) + \tilde{r}^2/S_*^2]^{\alpha}, \tag{18}$$

where

$$\Phi(r,z) = [\Psi_s - \Psi(r,z)]/(\Psi_s - \Psi_a),$$

$$P_0 = n_0 k_B T_0, \quad \tilde{r} = r/r_0,$$

$$S_* = \frac{1}{\sqrt{2\alpha}} \frac{r_0}{\lambda_{i0}} \frac{\Psi_s - \Psi_a}{\pi r_0^2 B_*}, \quad \lambda_{i0} = \frac{v_{Ti}}{\omega_{ci}},$$

$$v_{Ti} = \sqrt{k_B T_0/m_i},$$

$$\frac{\Omega_i}{\omega_{ci}} = \frac{1}{S_*^2} \frac{\Psi_s - \Psi_a}{\pi r_0^2 B_*}, \quad \omega_{ci} = \frac{q_i B_*}{m_i c},$$

where $T_i(r,z)$ is the ion temperature, $\Psi(r,z)$ is the poloidal magnetic flux, Ψ_s and Ψ_a are the value at the magnetic separatrix and the value at the field-null point, respectively, T_0, n_0, and P_0 are constant, B_* is the average magnetic field, r_0 is the device radius, and k_B is the Boltzmann constant. The second term in the brackets in Eqs. (16)–(18) represents the centrifugal potential, which increases in proportion to $1/S_*^2$. The centrifugal potential allows leakage of the plasma beyond the magnetic separatrix ($\Phi = 0$). The parameter $\bar{s}$ is related to S_* as

$$\bar{s} = S_* \frac{\sqrt{\alpha/2}}{\tilde{r}_s} \int_{\tilde{r}_a}^{\tilde{r}_s} \frac{-(d\Phi/d\tilde{r})d\tilde{r}}{(\Phi + \tilde{r}^2/S_*^2)^{1/2}}, \tag{19}$$

where $\tilde{r}_s = r_s/r_0$ and $\tilde{r}_a = r_a/r_0$. Figure 2 shows the dependencies of $\bar{s}$ and Ω_i/ω_{ci} on the parameter S_* for the case where $\alpha = 1.5$ and the separatrix length along the z axis z_s is equal to $3r_0$. The parameter $\bar{s}$ decreases monotonously as S_* decreases, and the relation $\bar{s} \approx 1$ holds when $S_* \approx 1$. The normalized angular velocity Ω_i/ω_{ci} increases in proportion to $1/S_*^2$. It is worthwhile to note that the centrifugal force acting on the ion fluid becomes comparable to the Lorentz force as $\bar{s}$ approaches 1 [see Eqs. (16)–(18)].

After having obtained a two-fluid equilibrium by solving Eqs. (11)–(15) numerically the position $\mathbf{x}(0)_j$ and the velocity $\mathbf{v}(0)_j$ of the jth particle are determined from the fluid quantities $P_i(r,z)$, $P_e(r,z)$, $n_i(r,z)$, $n_e(r,z)$, $U_i(r)$, and $U_e(r)$ by using the quiet start technique.[14] We adopt the boundary condition that the physical quantities are periodic at two axial edges of the cylindrical vessel ($z = 0$, z_v; z_v is fixed to $5r_0$ in this paper) and a particle is completely elastically reflected on the conducting wall ($r = r_0$). Both ions and electrons are treated as super-particles that have much larger masses and charges compared with the real masses and charges. The time step Δt is fixed to $2/\omega_{pe}$, where ω_{pe} is the average electron plasma frequency. The numerical scheme used for the three-dimensional particle simulation relies on a semi-implicit method.[12,13] One of the properties

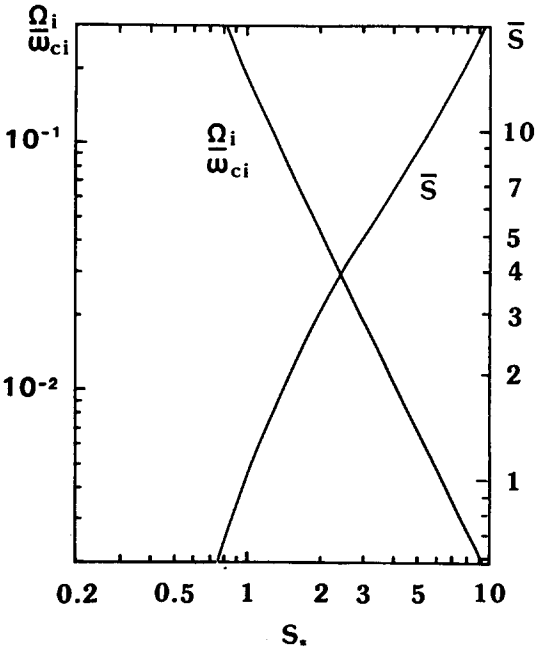

FIG. 2. The dependence of $\bar{s}$ and Ω_i/ω_{ci} on the parameter S_* in the cold electron model. The profile parameter α is assumed to be 1.5 and the separatrix length along the z axis z_s is fixed to $3r_0$. The scale on the left vertical axis measures Ω_i/ω_{ci} and the scale on the right vertical axis measures $\bar{s}$.

of this scheme is that high-frequency waves can be artificially damped by introducing a time-decentering technique and hence low-frequency phenomena can be described without dropping electron and ion FLR effects.

III. SIMULATION RESULTS

Four simulation runs with different values of $\bar{s}$ are carried out, where the total number of particles is fixed to 10^5. The simulation runs are terminated after one Alfvén transit time t_A, where t_A is defined by r_0/v_A and v_A is the average Alfvén velocity in the plasma region. The simulation parameters are listed in Table I. We obtain the initial profiles with different values of $\bar{s}$ by changing the value of the particle mass keeping the fixed mass ratio of $m_i/m_e = 40$.

A. Ion kinetic effect on tilt stabilization

Before considering the mechanism of tilt stabilization, let us start by describing the general feature of the particle motion in the FRC plasma. The initial profiles of the magnetic pressure, the poloidal magnetic field, the ion thermal pressure, and the ion mass density in the (r,z) plane are shown in Fig. 3 for $\bar{s} = 5$, where the radial scale is magnified by two times for convenience. The magnetic pressure has a steep gradient along the r direction while its value varies moderately along the z axis. In other words, the magnetic pressure is formed in a fairly prolate shape. The profile of the magnetic field strongly affects the particle behavior. Particularly in the vicinity of the field-null point a particle reveals fairly complex behavior. As a particle approaches the field-null point, the effect of the magnetic field on particle motion becomes reduced and thus a particle can move more freely.

TABLE I. Simulation parameters. The γ/γ_{MHD} column shows the growth rate γ normalized by the MHD value γ_{MHD} for $0.4t_A < t < t_A$ and the last two columns represent the anisotropies of the ion and electron pressures at $t = t_A$. The electron charge q_e used in the simulation is equal to $-q_i$. The parameters $m(=9.1\times10^{-28}$ g) and $e(=4.8\times10^{-10}$ esu) are the real mass and the real charge of an electron, respectively.

$\bar{s}$	m_i/m	m_e/m	q_i/e	v_{Ti}/c	λ_{i0}/r_0	γ/γ_{MHD}	P_{zi}/P_{ri}	P_{ze}/P_{re}
1.0	1.0×10^{6}	2.5×10^{4}	1.0×10^{5}	1.9×10^{-2}	1.9×10^{-1}	0.01	1.71	1.02
2.0	4.8×10^{5}	1.2×10^{4}	1.0×10^{5}	2.0×10^{-2}	9.5×10^{-2}	0.05	1.57	0.96
3.0	3.2×10^{5}	8.0×10^{3}	1.0×10^{5}	2.0×10^{-2}	6.3×10^{-2}	0.24	1.40	1.04
5.0	2.0×10^{5}	5.0×10^{3}	1.0×10^{5}	1.9×10^{-2}	3.8×10^{-2}	0.38	1.29	1.03

For example, a particle that exists inside the critical point ($x < 2\lambda_i$) takes a relaxed meandering orbit (see Fig. 1). We call this region the magnetic well for brevity. Then, most of the particles meander without any self-intersection in the magnetic well. The magnetic well has a fairly prolate shape corresponding to the profile of the magnetic pressure, although its width depends on the kinetic energy of each particle. We illustrate the spatial structure of the ratio of the local Larmor radius of the ion with the thermal energy to the scale length of the magnetic field at $t = 0$ in Fig. 4 for the cases of $\bar{s} = 1$ (left) and $\bar{s} = 5$ (right), where the dotted lines show contours less than 0.5 and the solid lines show contours larger than 0.5 (contours larger than 1.0 are not shown for clarity). It is clear from Fig. 4 that the prolate magnetic well is formed in the central plasma region and the area becomes wider as $\bar{s}$ decreases.

Figures 5 and 6 show the bird's-eye view (left) and the top view (right) of the orbits of 100 ions for the cases of $\bar{s} = 1$ (Fig. 5) and $\bar{s} = 5$ (Fig. 6), where each curve represents the ion trajectory during one Alfvén transit time from the start of simulation. For the case of $\bar{s} = 5$ the meandering orbit concentrates on a small region near the field-null line. An ion in the outer region moves on a gyration orbit with a relatively small gyroradius. On the other hand, most of the ions move about in the whole plasma region with a large meandering orbit for the case of $\bar{s} = 1$. Thus the number of particles with a meandering orbit increases as $\bar{s}$ approaches 1. This result indicates that most of the particles exist in the magnetic well for the case of $\bar{s} = 1$ and can move fairly freely without being restrained by the magnetic field. Incidentally, it should be noted that the number of meandering electrons is much smaller than that of meandering ions.

With the above preparation in mind let us examine the temporal evolution of the tilt mode by expanding the z component of the velocity field into the Fourier series. The dependence of the average growth rate on the parameter $\bar{s}$ is plotted in Fig. 7, where the average growth rate is calculated from the mode amplitude in the range $0.4t_A < t < t_A$, the open circle represents the value obtained by the simulation, and the closed triangles show the results of a linear theory.[7] The dashed line is drawn to represent the average tendency of the growth rate as a function of $1/\bar{s}$. The growth rate normalized by the MHD value[6] is also listed in the γ/γ_{MHD} column of Table I. The evolution of the tilt mode is completely suppressed when $\bar{s} \approx 1$. As $\bar{s}$ increases, the tilt mode tends to be more unstable and the growth rate approaches the MHD value. The behavior of the kinetic growth rate is in good agreement with the result of linear theory.[7] It can be concluded, therefore, that the stabilization effect resulting from the finiteness of the ion Larmor radius is very efficient

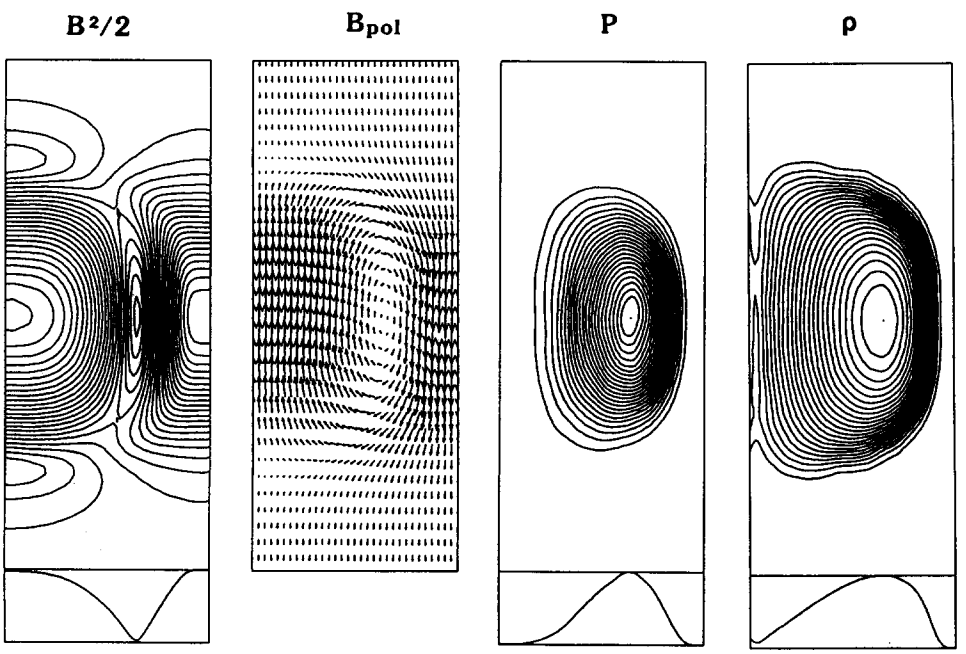

FIG. 3. The initial profiles of the magnetic pressure $B^2/2$, the poloidal magnetic field, the ion thermal pressure P, and the ion mass density ρ in the (r,z) plane for the case of $\bar{s} = 5$, where the radial scale is magnified by two times for convenience. The small bottom panel shows the radial distribution in the midplane of the upper panel.

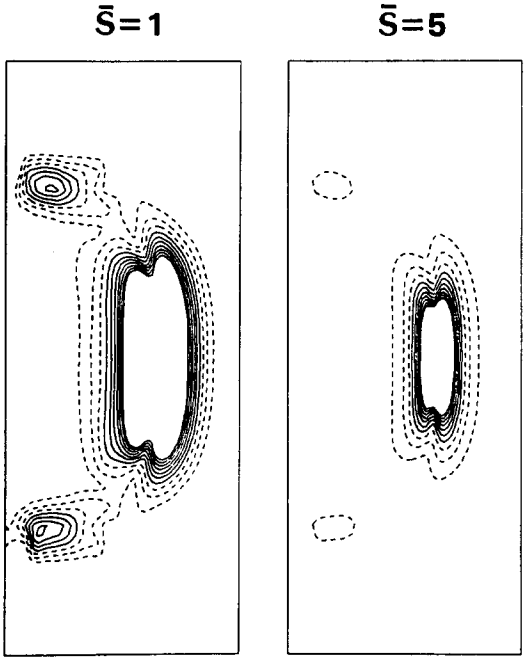

FIG. 4. The initial profiles of the ratio of the local ion Larmor radius to the scale length of the magnetic field for the cases of $\bar{s}=1$ (left) and $\bar{s}=5$ (right), where the radial scale is magnified by two times for convenience. The dotted lines show contours less than 0.5 and the solid lines show contours larger than 0.5 (contours larger than 1.0 are not shown for clarity).

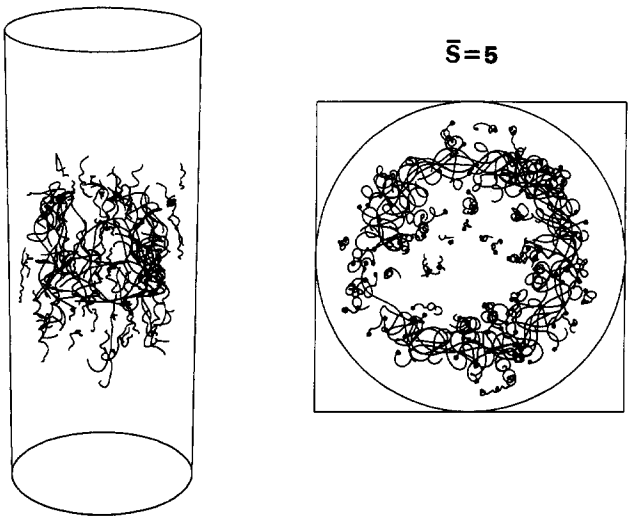

FIG. 6. The same as Fig. 5 for the case of $\bar{s}=5$.

for the FRC tilt mode.

We are now in a position to elucidate the physical mechanism of the ion kinetic effect on tilt stabilization. In doing so let us first consider the tilting instability for the MHD case. Suppose that a perturbation of the $n=1$ tilt mode is added to the initial two-dimensional equilibrium. The perturbation gives rise to an $n=1$ modification of the plasma current profile. A torque force is then generated by the vector product between the perturbed plasma current and the external field, whereby the tilt modification is accelerated. This comes from the fact that the MHD plasma is frozen in the magnetic field. On the other hand, for a kinetic plasma with $\bar{s}=1$ most of the ions are free from the constraint of the magnetic field and oscillate around the field-null point with a large amplitude, as was shown in Fig. 5. Suppose that the direction of the velocity of the tilting perturbation is in phase with that of the meandering oscillation of an ion. Then, the ion changes to a new oscillation orbit with a larger amplitude, but with the same oscillation center. When the direction of the perturbed velocity is opposite, the ion executes a

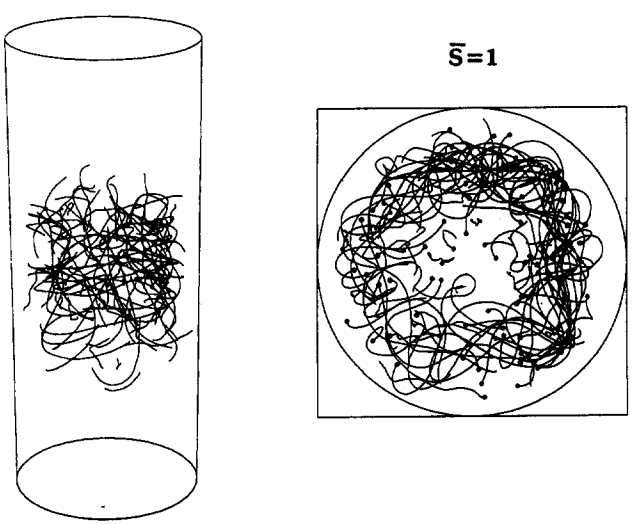

FIG. 5. The bird's-eye view (left) and the top view (right) of the orbits of 100 ions for the case of $\bar{s}=1$. Each curve represents the ion trajectory during one Alfvén transit time from the start of simulation and a closed circle is attached to each curve to show the starting point.

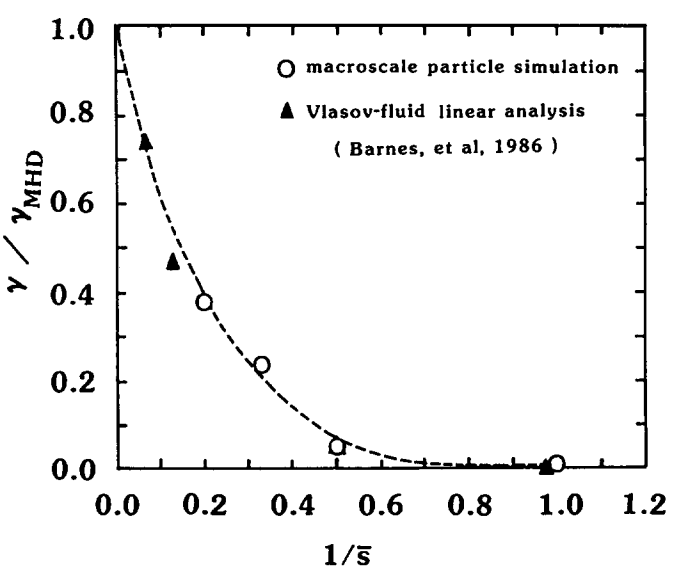

FIG. 7. The $\bar{s}$ dependence of the average growth rate of the tilting instability. The open circle represents the value obtained by the simulation and the closed triangles show the results of a linear theory calculated in Ref. 7. The dashed line represents the average tendency of the growth rate as a function of $1/\bar{s}$.

smaller amplitude oscillation, but the oscillation center remains the same in this case, as well. When the orbit is averaged over one oscillation period for either case, therefore, the toroidal current carried by the meandering ion does not contribute to the $n = 1$ tilt modification of the plasma current profile in the average. In other words, the ion with a meandering orbit does not contribute to the growth of the perturbation of the $n = 1$ tilt mode. Thus we conclude that the ion with a meandering orbit plays a key role in keeping the system stable against the tilting instability, and that the evolution of the tilt mode can be completely suppressed when most of the ions move on stable meandering orbits, i.e., when $\bar{s} \approx 1$. In this respect note that the drift direction of the meandering ions is the same as the direction of the ion diamagnetic current, though the gradient-**B** drift is opposite (see Fig. 1); this supports the above argument that the meandering ions contributing to the toroidal current play a vital role in tilt stabilization.

B. Anisotropy of pressure profile

The profiles of the ion distribution and the electron distribution in the velocity space are shown in Figs. 8 (ion) and 9 (electron) for the case of $\bar{s} = 2$, where the top panels show the initial distributions in the (v_r, v_z) plane (left) and in the (v_ϕ, v_z) plane (right), and the bottom two panels show the distributions at $t = t_A$. The dashed lines represent the coordinate axes and the dotted line represents the average value

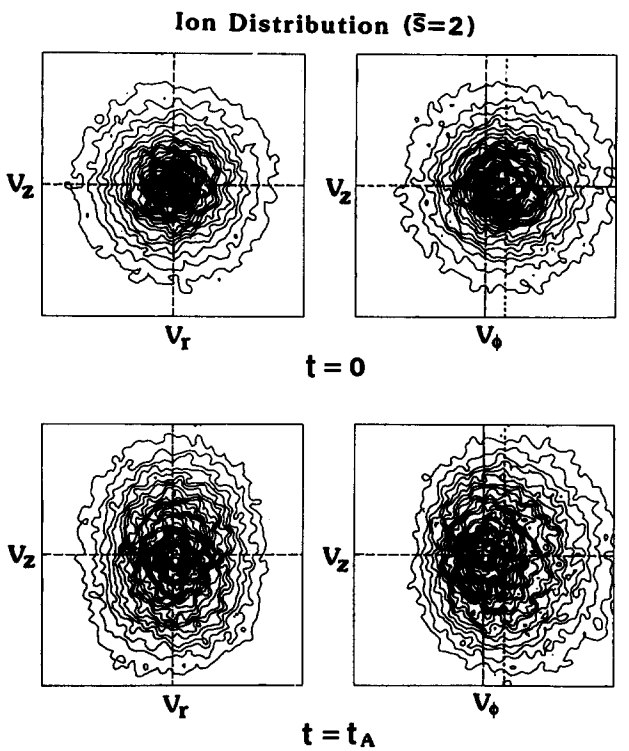

FIG. 8. The ion distribution in the velocity space for the case of $\bar{s} = 2$. The top panels show the initial distributions in the (v_r, v_z) plane (left) and in the (v_ϕ, v_z) plane (right), and the bottom two panels show the distributions at $t = t_A$. The dashed lines show the coordinate axes and the dotted line shows the average value of the ion toroidal velocity $\langle v_\phi \rangle$.

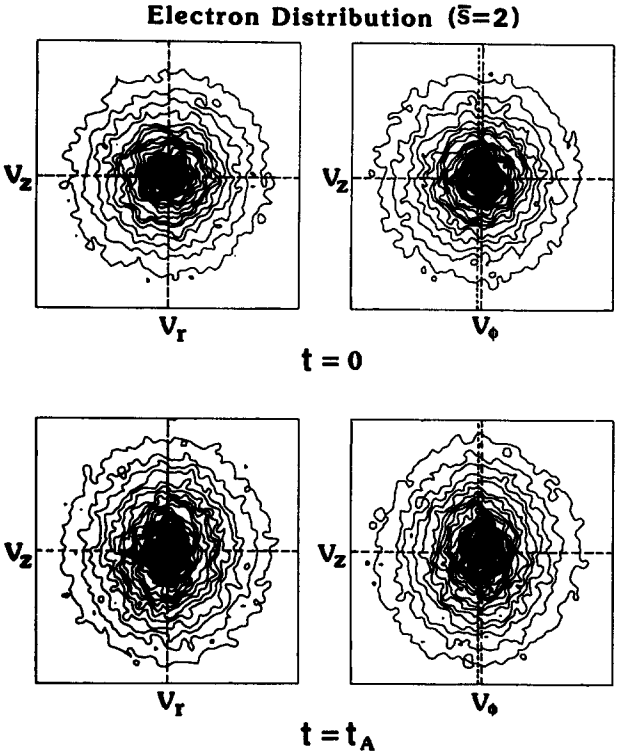

FIG. 9. The electron distribution in the velocity space for the same case as Fig. 8. The top panels show the initial distributions in the (v_r, v_z) plane (left) and in the (v_ϕ, v_z) plane (right), and the bottom two panels show the distributions at $t = t_A$. The dashed lines show the coordinate axes and the dotted line shows the average value of the electron toroidal velocity $\langle v_\phi \rangle$.

of the toroidal velocity $\langle v_\phi \rangle$. The ion distribution, which is isotropic at $t = 0$, changes to a distribution with an anisotropic temperature of $T_z > T_r$, T_ϕ after one Alfvén transit time, while the electron distribution remains almost isotropic during the simulation run.

This phenomenon can easily be explained by the anisotropic meandering orbit. As was mentioned before, a prolate magnetic well with a steep wall along the r direction is formed in the FRC plasma. A particle that can execute an oscillation in the z direction has a smaller energy compared with a particle that can execute an oscillation in the r direction, because the scale height x_0 in the z direction is larger than that in the r direction. (Note that the characteristic value of magnetic field B_0 varies in proportion to $1/x_0^2$ if the poloidal magnetic flux inside the radius x_0 is conserved.) Accordingly, the particles with the z oscillation predominantly exist in the prolate magnetic well and an ion distribution with an anisotropic temperature of $T_z > T_r$ is realized in the FRC plasma.

Since the pressure anisotropy is deeply connected with the number of meandering particles, it is expected that the pressure profile approaches an isotropic one as the number of meandering particles decreases. The last two columns of Table I show the ion pressure anisotropy P_{zi}/P_{ri} and the electron pressure anisotropy P_{ze}/P_{re} at the plasma center for the runs with four different values of $\bar{s}$. As can be clearly seen, the ion anisotropy is roughly inversely proportional to $\bar{s}$ while the electron distribution remains almost isotropic

regardless of $\bar{s}$. Thus we can conclude that the pressure anisotropy is caused by the anisotropy of the meandering orbit.

C. Plasma rotation

Finally, we shall examine the structure of the average toroidal (ϕ) flow. We can find in Fig. 8 that only the high-energy ions shift in the positive ϕ direction at $t = t_A$, in spite of the fact that all the components have had a positive toroidal shift at $t = 0$. This means that the greater part of the toroidal ion (positive ϕ) current is carried by the meandering ions. In this respect one should note that the drift direction of the meandering ions is reversed in comparison with that of the gradient-B drift when $\lambda_i/x_0 > 0.303$; more specifically, the drift direction of the meandering ions becomes the same as the direction of the toroidal current, thus positively contributing to the toroidal current.

Figure 10 shows the temporal evolutions of the Mach numbers of the ion toroidal flow (positive) and the electron toroidal flow (negative) for runs with four different values of $\bar{s}$, where the Mach number is calculated at the field-null point. The Mach number of the electron flow is plotted in the negative region of Fig. 10 because the average electron flow always moves in the negative ϕ direction. The fact that the average velocity of the electron toroidal flow is always negative is attributed to the electron diamagnetic drift. The Mach number of the ion toroidal flow changes approximately inversely proportional to the value of $\bar{s}$ and the rotational velocity of the ion flow reaches a value a little larger than half the thermal velocity for the case of $\bar{s} = 1$. If the orbit motion is averaged over one oscillation period, the meandering orbit with no self-intersection has a larger average toroidal velocity than the drift orbit with self-intersection (see Fig. 1). Therefore the average fluid velocity along the field-null line increases as the parameter $\bar{s}$ decreases, that is, the number of the meandering particles increases. It should be noted that the rotation speed obtained here is much smaller than the threshold value for the spin stabilization evaluated by using the MHD simulation,[6,15] thus indicating that the stabilization effect observed in our simulation study is not due to the spin effect.

The spatial structure of the ion toroidal flow velocity is shown in Fig. 11 for the case of $\bar{s} = 3$, where the top perspective diagram represents the initial structure in the (r,z) plane and the bottom diagram represents the final structure. A rigid rotor is assumed in the initial equilibrium profile. As time elapses, the initial profile is modified and the high-speed component appears near the top and bottom edges where the field lines are sharply curved. By examining the property of the magnetic curvature drift in the final profile it is found that both the spatial structure and the amplitude of the magnetic curvature drift are in good agreement with those of the modified ones. As the number of the meandering ions increases, the difference from the rigid rotor is reduced. We note here that the development of the $n = 2$ rotational instability is not observed for any case in one Alfvén transit time.

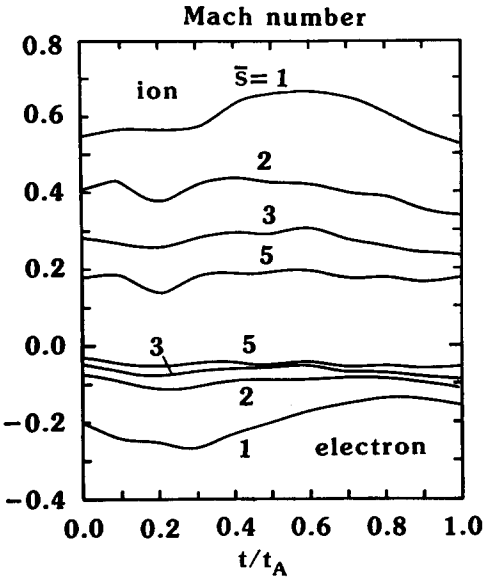

FIG. 10. The time histories of the Mach numbers of the ion toroidal flow (positive) and the electron toroidal flow (negative) for the cases where $\bar{s}$ is equal to 1, 2, 3, and 5, respectively. The Mach number is calculated at the field-null point. The Mach number of the electron flow is plotted in the negative region because the average toroidal electron velocity is always negative.

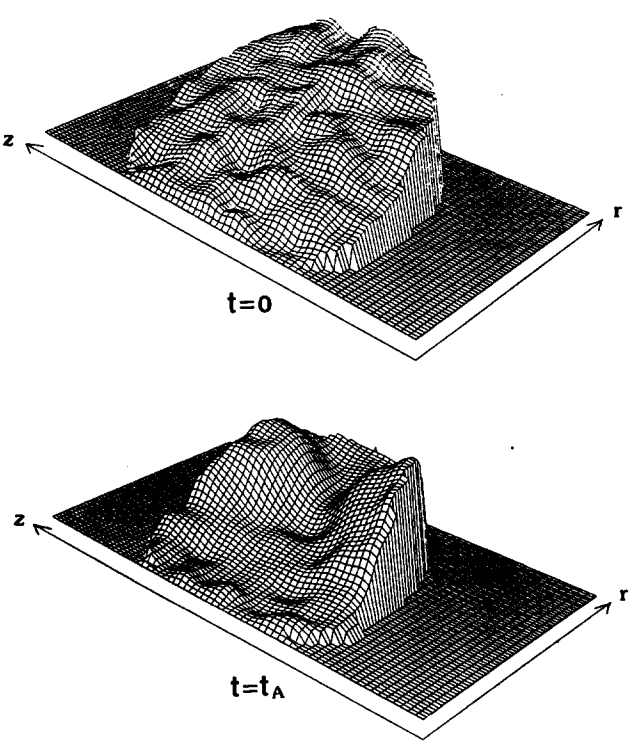

FIG. 11. The perspective diagrams of the ion toroidal flow velocity at $t = 0$ (top) and $t = t_A$ (bottom) for the case of $\bar{s} = 3$. Here, the vertical axis shows the toroidal velocity in the (r,z) plane, which is averaged in terms of the ϕ variation.

IV. SUMMARY AND DISCUSSION

In order to investigate the ion kinetic stabilization effect on the tilting instability in the FRC plasma we have devel-

oped a three-dimensional particle simulation code that can describe both microscale particle motions and magnetohydrodynamic evolutions in cylindrical coordinates. By carrying out four simulation runs with different values of $\bar{s}$ we have been able to clarify the role of the ion kinetic effects on the stabilization of the FRC tilt disruption. The main results can be summarized as follows.

(a) The growth rate of the tilting instability decreases as the parameter $\bar{s}$ decreases and the instability is completely suppressed when $\bar{s} \approx 1$. This kinetic stabilization effect is attributed to the characteristics of the ions that execute meandering motions around the field-null line. The meandering ion orbit shifts to an orbit with a slightly larger/smaller oscillation amplitude; however, the average behavior of the meandering ions does not contribute to the tilt modification of the plasma current because of their oscillatory motion around the same oscillation center. As $\bar{s}$ becomes smaller, the number of meandering ions increases and thus the ion kinetic stabilization becomes more efficient.

(b) The meandering ion preferably oscillates along the z direction because of the existence of a prolate magnetic well with a steep magnetic wall along the r direction. The anisotropy of the meandering orbit results in the anisotropy of the ion pressure profile. The degree of the anisotropy decreases as the number of meandering ions decreases.

(c) The toroidal ion current is mainly carried by the meandering ions with high energy. The ion toroidal flow velocity increases as $\bar{s}$ decreases and the Mach number is nearly equal to 0.5 for the case of $\bar{s} = 1$. The spatial profile of the plasma rotation is modified by the magnetic curvature drift at the sharply curved edges of field lines. The modification becomes smaller as the number of meandering ions increases.

Most FRC plasmas have been produced with lifetimes of many Alfvén transit times in the small $\bar{s}$ region ($\bar{s} \leqslant 2$). Our result is in good agreement with these small $\bar{s}$ experiments. Slough and Hoffman,[10] however, reported that FRC plasmas were experimentally produced with a large $\bar{s}$ (≈ 5) and these lifetimes were as long as 10–20 kinetic growth times. This paper can not give a clear answer to the question why a large $\bar{s}$ plasma can persist for such a long time without suffering from the tilting instability. One explanation may come from the fact that the formation of FRC plasma is followed by a strong dynamical axial implosion. That is, this fact suggests the possibility that the energy released from the dynamical motion can make an experimental equilibrium different from the numerical solution used in this paper.

Let us briefly touch on the role of the electric field on the tilt stabilization. We have obtained the initial equilibrium by assuming that the electric field would not play an essential role in the global instability, such as the tilt mode. The temporal evolutions of the electric field energy in the present study are shown in Fig. 12 for four different $\bar{s}$ cases. Here, the electric field is expressed in such a normalized unit that the average magnetic field is nearly equal to 1. It is clear in Fig. 12 that the electric field remains at a considerably lower level compared with the magnetic field for the four cases, though the values slowly change in time and have $\bar{s}$ dependence. Thus we can conclude that the electric field cannot play an essential role in the stability of the tilt disruption.

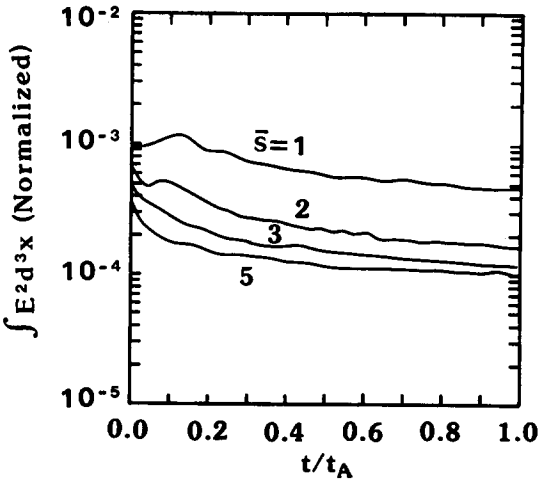

FIG. 12. The time histories of the electric field energy for the same cases as Fig. 10 where the electric field is obtained in a normalized unit.

Before concluding this paper let us discuss the applicability of the model developed here. In general, the numerical error appears in the form of thermal noise resulting from the finiteness of the number of the particles used in the simulation. In this paper we dealt with 10^5 particles. The number of the particles in a cell is around 20 at the central region of the FRC plasma, while there are only a few particles in a cell near the plasma boundary. Therefore numerical noise tends to be created at the boundary of the FRC plasma. In order to reduce the numerical effect from the simulation we used a low-pass filter.[6] As a result the fluctuation level of the numerical noise is kept always at less than 10% of the tilt mode. As far as the tilting instability is concerned, the influence of the numerical noise is therefore not predominant. If one wishes to investigate the phenomenon in the edge region, a simulation with many more particles will be needed.

We have obtained the initial condition by solving the two-fluid MHD equilibrium. As $\bar{s}$ approaches 1, a discrepancy between the MHD equilibrium state and the particle equilibrium state appears because of the ion finite-Larmor radius effect. In order to exclude the influence of this discrepancy from the simulation results the analysis of the tilt mode is carried out after the plasma configuration is relaxed to a quasiequilibrium state in the simulation ($t > 0.4 t_A$). An alternative method is to solve the Maxwell–Vlasov equations and start the simulation from the solution. However, it is fairly difficult to solve the two-dimensional Maxwell–Vlasov equations in cylindrical coordinates because of the highly nonlinear nature. We hope that these problems will be solved elsewhere.

ACKNOWLEDGMENTS

We are grateful to Professor K. Nishikawa for his continuous interest in this work and Dr. M. Tanaka for his kindness in allowing us to use his semi-implicit particle simulation scheme.

This work is supported by a Grant-in-Aid for Fusion Research from the Japanese Ministry of Education, Science, and Culture.

[1] S. Ohi, T. Minato, Y. Kawakami, M. Tanjyo, S. Okada, Y. Ito, M. Kako, S. Goto, T. Ishimura, and H. Ito, Phys. Rev. Lett. **51**, 1042 (1983); A. L. Hoffman, J. T. Slough, and D. G. Harding, Phys. Fluids **26**, 1626 (1983).
[2] W. N. Rosenbluth and M. N. Bussac, Nucl. Fusion **19**, 489 (1979); J. H. Hammer, *ibid.* **21**, 488 (1981).
[3] J. L. Schwarzmeier, D. C. Barnes, D. W. Hewett, C. E. Seyler, A. I. Shestakov, and R. L. Spencer, Phys. Fluids **26**, 1295 (1983).
[4] R. A. Clemente and C. E. Grillo, Phys. Fluids **27**, 658 (1984).
[5] See, for example, A. G. Eskov, R. Kh. Kurtmullaev, A. P. Kreshchuk, Ya. N. Laukhin, A. I. Malyutin, A. I. Markin, Yu. S. Martyushov, B. N. Mironov, M. M. Orlov, A. P. Proshletsov, V. N. Semenov, and Yu. B. Sosunov, in *Plasma Physics and Controlled Nuclear Fusion Research 1978*, Proceedings of the 7th International Conference (IAEA, Vienna, 1979), Vol. 2, p. 187; W. T. Armstrong, D. G. Harding, E. A. Crawford, and A. L. Hoffman, Phys. Fluids **25**, 2121 (1982).
[6] R. Horiuchi and T. Sato, Phys. Fluids B **1**, 581 (1989).
[7] D. C. Barnes, J. L. Schwarzmeier, H. R. Lewis, and C. E. Seyler, Phys. Fluids **29**, 2616 (1986).
[8] A. Ishida, H. Momota, and L. C. Steinhauer, Phys. Fluids **31**, 3024 (1988).
[9] R. D. Milroy, D. C. Barnes, R. C. Bishop, and R. B. Webster, Phys. Fluids B **1**, 1225 (1989).
[10] J. T. Slough and A. L. Hoffman, Nucl. Fusion **28**, 1121 (1988).
[11] J. S. Kim and J. R. Cary, Phys. Fluids **26**, 2167 (1983).
[12] M. Tanaka and T. Sato, Phys. Fluids **29**, 3823 (1986).
[13] M. Tanaka, T. Sato, and A. Hasegawa, Phys. Fluids B **1**, 325 (1989).
[14] C. K. Birdsall and A. B. Langdon, *Plasma Physics Via Computer Simulation* (McGraw-Hill, New York, 1985).
[15] R. D. Milroy, D. C. Barnes, R. C. Bishop, and D. D. Schnack, in *Proceedings of the 12th Conference on the Numerical Simulation of Plasmas* (Lawrence Livermore National Laboratory, Livermore, CA, 1987), Abstract PM21.